A combined computational and experimental characterization of lean premixed turbulent low swirl laboratory flames. I. Methane flames.

Marc Day[1a], *Shigeru Tachibana*[2], *John Bell*[l], *Michael Lijewski*[1],
Vince Beckner[1] *and Robert Cheng*[3],

[1] *Center for Computational Sciences and Engineering, Lawrence Berkeley National Laboratory, Berkeley, CA, USA*

[2] *Japan Aerospace Exploration Agency, Tokyo, Japan*

[3] *Environmental and Energy Technologies, Lawrence Berkeley National Laboratory, Berkeley, CA, USA*

[a] *Corresponding Author - contact*: *MSDay@lbl.gov, (510) 486-5076*

Abstract

This paper is the first in a series that presents a combined computational and experimental study to investigate and characterize the structure of premixed turbulent low swirl laboratory flames. The simulations discussed here are based on an adaptive solution of the low Mach number equations for turbulent reacting flow, and incorporate detailed models for transport and thermo-chemistry. Experimental diagnostics of the laboratory flame include PIV and OH-PLIF imaging, and are used to quantify the flow field, mean flame location, and local flame wrinkling characteristics. We present a framework for relating the simulation results to the flame measurements, and then use the simulation data to further probe the time-dependent, 3D structure of the flames as they interact with the turbulent flow. The present study is limited to lean methane-air flames over a range of flow conditions, and demonstrates that in the regime studied, local flame profiles are structurally very similar to the flat, unstrained steady ("laminar") flame. The analysis here will serve as a framework for discussing a broader set of premixed flames in this same configuration. Papers II and III will discuss corresponding analysis for pure hydrogen-air and hydrogen-methane mixed fuels, respectively.

Keywords: Premixed turbulent combustion; direct numerical simulation; flamelet analysis; lean premixed methane-air; low swirl burner

1 Introduction

In the past two decades, lean premixed combustion has become the leading technology for controlling NO_x emissions. Modern premixed combustion systems are highly optimized to exploit specific properties of fuels such as natural gas or propane. However, with an increasing need to reduce green house gas emissions, the next-generation combustion systems will have to operate efficiently and safely with a multitude of fuels that will be derived from the gasification of coal and biomass, and from other renewable fuel sources. The compositions of these alternate fuels will vary significantly with the type of feedstocks and their treatment processes, but are likely to be composed primarily of hydrogen, hydrocarbons, carbon monoxide, water vapor, and inert gases such as, nitrogen, and carbon dioxide. New fuels with significant hydrogen composition are particularly interesting for low emissions applications. For example, H_2 concentrations of up to > 90% are expected in fuels proposed for the integrated gasification combined cycle coal power plants with carbon capture and storage capability. The device exploits the enhanced chemical reactivity and transport properties of hydrogen in order to support ultra-lean flames, which are beneficial from an emissions standpoint. Similarly, low levels of hydrogen addition have been shown to extend the flammability ranges in more traditional fuels, by promoting or increasing the fuels chemical reactivity. However, the same thermo/diffusive properties of hydrogen that support leaner flames in mixed-fuel scenarios lead to more profound issues in the limit of pure hydrogen-air mixtures, because they lead to thermo/diffusive instabilities which have a dramatic impact on flame propagation, heat release and the general predictability of these systems. Little is known about the interaction of these types of instabilities with turbulence in practical devices, and to what extent they are suppressed in hydrocarbon/hydrogen fuel blend scenarios. A better understanding of the fuel effects on the fundamental premixed turbulent flame properties is critical to the development of fuel-flexible premixed combustion systems, and the role of hydrogen on these systems appears to be of central importance. Such effects have not yet been fully characterized and incorporated into turbulent flame models appropriate for design and analysis.

This paper is the first in a series that presents a combined computational and experimental study to investigate and characterize the structure of premixed turbulent

CH_4/H_2 flames. The complete study consists of lean CH_4/air flames that are thermal/diffusive neutral (Lewis number, Le ≈ 1), lean H_2/air flames (Le < 1) that are thermal/diffusive unstable, and several mixed flames with stability properties intermediate to those of the two extremes. In this paper, we introduce the computational approach used to simulate the entire class of relevant laboratory-scale flames, and then discuss a number of diagnostics that validate the simulations with data taken from a laboratory experiment. The simulation and analysis procedures are directly applicable to the broader class of flames in the study. However, turbulent flames burning in the hydrogen-seeded mixtures are treated separately because analysis of the diagnostics is significantly more complex due to the thermal/diffusive instability of the fuel.

Our previous investigations of Lewis number effects in simplified configurations will provide the framework for the current analysis [1, 2]. In both this study and in the previous work, we employ a low Mach number formulation of the time-dependent reacting flow equations, and use adaptive mesh refinement (AMR) to evolve the system numerically. By combining the low Mach number model with AMR, the simulations can cover a physical domain that is an order of magnitude larger in each dimension than typical reacting flow direct numerical simulations (DNS) to date using comparable resources, while at the same time enabling the structure of the flame to be resolved using detailed models for the chemical kinetics and molecular transport.

In Reference [1] a computational study presents the dependence of flame structure with fuel Lewis number in a rectangular domain. The 2D configuration employed inflow/outflow boundaries in the coordinate direction aligned with the mean flow and flame propagation. (The domain was periodic in the transverse direction.) During those simulations, the mean inlet velocity was adjusted dynamically using an automatic control algorithm to maintain the mean flame position at a fixed distance above the inflow face. Low-amplitude velocity fluctuations were superimposed on the mean inlet flow and the resulting flames were analyzed to assess the effect of time-dependent turbulent-like straining on the detailed flame structures. The resulting lean CH_4 and C_3H_8 flames exhibited local heat release characteristics that were similar to those of the corresponding steady unstrained 1D idealized flames. A flame in a lean H_2–air mixture, however, showed considerable increases in the local heat release rate over the much of the flame,

as well as significant variation in the local heat release and fuel consumption rates, even in regions that were locally flat. It was shown that this thermal/diffuse unstable flame was not easily characterized in terms of the 1D steady unstrained idealization. Essential properties of the mean and instantaneous flame structure were inherently multi-dimensional and time-dependent.

A subsequent 3D computational study, also in an idealized configuration [2] explored the thermal/diffusive instability effects of lean H_2–air flames over a range of low-level turbulence intensities. In that study, cellular patterns of fuel consumption and flame propagation were observed as they interacted with the evolving turbulent flow field. Local flame propagation speeds (based on consumption rates integrated normal to the flame surface) were considerably higher in localized pockets than in the corresponding idealized flat flame (i.e., an unstrained steady idealized flame with identical upstream conditions). The enhancement in consumption speed is attributed to localized fuel enrichment that resulted from differential diffusion processes. Enhanced global fuel consumption rates were attributed to the combination of increased flame surface area and intensified local consumption. Considerable variability was observed in this 3D case, qualitatively similar to that observed in the 2D studies. The main implication of this work, practically, is that estimates of the turbulent flame speed as the product of flame surface area and laminar flame speed[1] significantly under-predict the overall heat release rate in these mixtures.

The present studies involve 3D time-dependent simulations of laboratory-scale flames. In particular, we look at flames generated by a low-swirl burner (LSB) [3-5]. Similar to our previous laboratory-scale computational flame studies, e.g., a turbulent V-flame [6] and a piloted slot Bunsen burner [7], the goal here is to understand and characterize turbulence/flame interactions at the correct physical scales of laboratory experiments. For premixed burners, this may be a key feature, since burners with different flame stabilization methods emphasize distinct aspects of the interplay between the mean and fluctuating flow features and the flame propagation. Historically, it has

[1] The "laminar flame speed" is the propagation speed of a steady unstretched flame propagating into a quiescent fuel of the same mixture. The "thermal thickness"is the width of such a flame, defined as the inverse of the peak thermal gradient scaled by the change in temperature from fuel to products

been very difficult to characterize the wide range of experimental configurations with flames in a generic (device-neutral) context [8]. High-fidelity simulations capable of capturing the interplay between the flow and chemistry at realistic experimental device scales can therefore play an important role in providing useful insights for the development of turbulence and flame models to improve the fidelity of computational design tools for engineering systems, and will be of great aid in constructing the sort of device-neutral characterizations that are presently lacking.

The LSB establishes a divergent turbulent flow of reactants that aerodynamically stabilizes a detached freely-propagating premixed flame (Fig. 1). The outer swirling component of the mean flow interacts with the ambient air in the outer shear region; however, the central region of the LSB, which is essentially isolated from the outer flow is devoid of complex large scale flow structures, such as an intense recirculation zone or coherent bulk motions. Notably, the LSB flame does not require an additional energy source such as a pilot flame at very lean fueling conditions in order to maintain flame stability. Also, self-similarity of the divergent flowfield enables the LSB device to operate over a wide range of fuel mixtures, flow velocities, equivalence ratios, device pressures and fuel temperatures. This robustness allows lean methane and hydrogen fuels to be studied at similar inflow and turbulent conditions [9].

In the present work, we will compare simulation results with velocity statistics that are measured in the laboratory using particle image velocimetry (PIV). Flame front topologies are measured using planar laser induced fluorescence of OH radicals (OH-PLIF). To extract 3D time dependent flame information from numerical simulations of these flames, we consider two different approaches for the analysis. One approach is based on tracking Lagrangian pathlines through the reacting fronts [10]. The second type of analysis is based on a more traditional approach in which we construct a local coordinate system in a neighborhood of the flame [2]. Although these diagnostics provide a somewhat different view of the flame, for CH_4 flames, which are near unity Lewis number, we expect the results to be quite similar. Here, we demonstrate that similarity by reporting conditional scalar measurements using both types of diagnostics. For flames fueled by H_2-air mixtures that will be discussed in subsequent papers in this series, these two approaches provide somewhat different and complementary information. We also

use the Lagrangian pathlines to investigate time dependent stretch effects as fluid parcels pass through the flame. We discuss how these results can be used as the baseline for comparison with flames in more complex mixtures.

2 Burner configuration:

The LSB configuration used for our studies (Fig. 2) was developed jointly with Lund Institute of Technology, and Technical University Darmstadt [5] to facilitate the collection of a broad and consistent premixed turbulent flame database for the validation of computational results. The benefits of the LSB are its well-characterized inflow and boundary conditions. For atmospheric flames open to the laboratory environment, a lifted flame is produced that is amenable to measurements of velocity, temperature, and species concentrations using laser diagnostics. The LSB nozzle has an inner diameter of 50 mm, with a swirler placed 68 mm upstream of its exit plane. The annular section of the swirler is fitted with eight constant thickness curved vanes, each having a discharge angle of 37^o. The central channel is 38 mm in diameter, and is fitted with a perforated plate that has 37 holes of 3 mm diameter. The holes are arranged in a hexagonal/radial pattern. The geometric swirler number of this LSB is 0.55 according to the measurements given in Ref. [5]. The flames generated by this LSB are slightly asymmetric at the lower velocity range (3 m/s < U_0 < 10 m/s) that we have investigated (see Fig. 1). This is caused by the transitional nature of the flow at these velocities, as discussed in detail in Appendix A, along with issues related to misalignment of the vanes (octagonal symmetry) with the holes in the perforated plate (hexagonal symmetry).

Physical constraints at LBNL do not permit the installation of the 60 cm wide co-flow air shroud (at 0.3 m/s) that is used at comparable facilities at Lund and at Darmstadt to prevent the entrainment of dust particles that degrade their Raman and Rayleigh scattering signals. This shroud is not essential for the analysis of our PIV and OH-PLIF measurements, which is focused on flows near the axis of the device. To verify that the overall characteristics of our LSB are consistent with the ones at the other two institutions, we conducted a PIV study of the non-reacting flows at flow velocities of U_0 from 3 to 18 m/s and the LSF-1 flame (CH_4/air at ϕ = 0.62, U_0 = 6.2m/s) of Ref. [5]. The nearfield flow features obtained at LBNL are consistent with those of the non-reacting and reacting flows reported in Ref. [5]. Details of the non-reacting flows are presented in

Appendix A and show that the flowfield assumes self-similarity when $U_0 > 10$ m/s. This means that results reported by Petersson et al [5] at $U_0 = 6.2$ m/s were made in transitional flows. This observation is critical to the analysis that follows here, and may explain observations reported in the reference on the dominance of the inner shear layer on the flame stabilization process.

3 Numerical simulation:

The numerical simulation uses the low Mach number adaptive mesh refinement code, LMC, documented in Ref.[11]. The LMC code integrates the multi-species Navier-Stokes equations with chemical reactions, treating the fluid as a mixture of perfect gases, and using a mixture-averaged model for differential species diffusion. Soret, Dufour and radiative transport is ignored. The low Mach number approximation [12, 13] exploits the natural separation of velocity scales in this low Mach number flow, removing acoustic wave propagation from the analytic description of the system. Bulk compressibility effects due to chemical reaction and thermal conduction remain in the description but appear as a global constraint on the evolution of the velocity field. A predictor-corrector procedure is used that is based on a density-weighted projection scheme [14]. For the species conservation equations a temporal splitting method is used that incorporates a stiff ODE integration technique to handle the disparate time scales associated with detailed kinetics, transport and advection. Time evolution of the overall scheme is constrained by the fluid velocity rather than the acoustic wave speed, increasing the allowable numerical time step by a factor of approximately 10-20 compared to that required for traditional simulation approaches based on the compressible flow equations.

The adaptive implementation of LMC is based on a block-structured adaptive mesh refinement (AMR) strategy. In this approach, regions to be refined are organized into rectangular patches, with several thousand grid points per patch. One is thus able to use well-characterized rectangular grid methods to advance the solution in time; furthermore, the overhead in managing the irregular data structures is amortized over relatively large amounts of floating-point work. Adaptive refinement is performed in time as well as in space; each level of refinement is advanced at its own time step, subject to the constraint that the time step at a coarse level be an integral multiple of the time step at the next finer level. A synchronization strategy ensure discrete conservation and

various elliptical constraints are enforced across all refinement levels during the simulation. Grid refinement criteria based on the evolving solution are used to dynamically adjust the location of the fine grids as the computation proceeds. For this study, refinement was focused around the flame front and in the turbulent fuel stream between the nozzle and the flame. In spite of the algorithmic complexity and overhead, the AMR strategy resulted in more than an order of magnitude savings in computational resources compared to a uniform fine grid calculation of the same effective resolution.

LMC runs on distributed-memory parallel architectures using a dynamic load balancing algorithm that accommodates the changing workload as regions of refinement are created and destroyed during the computation. Here the load-balancing problem is complicated by the heterogeneous workloads associated with chemical kinetics. The overall scaling behavior of the code, in conjunction with the efficiency gains resulting from the low Mach number formulation and the use of adaptive refinement makes this code ideally (and uniquely) suited for this study.

4 Computational Setup

There are at least two approaches to treat the LSB nozzle in our type of simulation. One possibility is to include the flow generated in the nozzle as part of the simulation; the alternative is to use measured data to prescribe the flow at the nozzle exit. In a series of studies [15-17] considered both options in the context of LES simulations of lean methane-air mixtures. Considerably better agreement was found between simulated and measured profiles when the flow generated inside the nozzle was included. In particular, the simulations correctly predicted large-scale structures emanating from the swirl vanes, and these structures ultimately played a key role in stabilizing their flame. More generally, these results suggest that if experimental data is being used to define input conditions for a detailed flow simulation then a more detailed experimental characterization of the nozzle flow in terms of both mean profiles and turbulent fluctuations is needed.

For the present simulations we incorporate an experimental characterization of the flow at the nozzle exit similar to that used in the Nognmeyr studies. Stereoscopic-PIV is not available at LBNL, so the 3D PIV data obtained by Petersson et al. were used [5]: mean velocity profiles were specified as functions of radius from the device centerline

based on a lean ($\phi = 0.62$) CH_4 flame at a mean fueling rate of $U_0 = 6.2$ m/s. We note that the experimental data showed significant azimuthal variations; clear imprints of the 8 swirl vanes are easily discernable in PIV data taken in a horizontal plane here the nozzle exit. Profiles of mean velocity in the experiment were formed by averaging the experimental measurements taken on two vertical PIV imaging planes: one that aligned with the swirl vanes, and one that was midway between a pair of them. To generate the simulation inlet data at $U_0 = 10$ and 15 m/s, the averaged flow profiles were scaled linearly to match the mean fueling rate while preserving the effective swirl number. As discussed in the Appendix, such a scaling is only expected to be valid for data obtained at $U_0 = > 10$ m/s.

Turbulent fluctuations in the nozzle were created for the simulation in an auxiliary calculation and were superimposed on the mean flow profiles in order to simulate the effect of the upstream turbulence-generation plates. To do this, a zero-mean velocity field was generated that was representative of flow through a perforated plate (ie, an array of small jets). The flow was evolved numerically in a triply-periodic domain until the measured integral length scale in the direction of the jets was 4 mm, consistent with experimental measurements taken at the core region of the nozzle in inert flow. The resulting turbulent flow field was then superimposed on the experimental profiles of mean flow, assuming a Taylor hypothesis [18]. A radial scaling factor was used to shape the synthetic fluctuations to the mean measured turbulence intensity profiles.

The cubic computational domain for the reacting flow simulation measures 25 cm in each dimension. We implicitly assume that the boundaries of this box are sufficiently far from the flame that it has no affect on the dynamics. The exit of the LSB nozzle is centered on the base plane of the computational domain, and provides the time-dependent inflow of turbulent swirling flow. Outside the LSB nozzle, a 0.35 m/s upward coflow of cold air is specified. Note that this coflow configuration is consistent with the Lund experiment but not with the LBNL configuration. Numerically, the small coflow helps to economize the computation time required to flush the initial transient data from the simulation domain without adversely affecting the swirling flow and flame stabilization in the core region.

In the simulations, we consider two inflow velocities, 10 m/s and 15 m/sec, corresponding to cases M-C and M-D in Table 1 below. For each case the base mesh for the simulation is a uniform grid of 256^3 cells. Three additional levels of factor-of-two grid refinement are used to dynamically track regions of high vorticity (turbulence) and chemical reactivity (flame zone). For reference, the thermal thickness of the $\phi = 0.7$ CH_4-air flames simulated in this study (Table 1) is approximately 600 microns. The AMR refinement strategy was such that regions of nontrivial fuel consumption (i.e., the "flame zone") were contained entirely within the finest level at all times. The effective resolution in a neighborhood of the flame was thus 2048^3 cells. We ran the simulations from an arbitrary initial condition until the flame became statistically stationary (as indicated by the total inventory of fuel in the domain). We then continued the simulations to collect flow and flame statistics. Case M-C consumed approximately 850K node hours on the Franklin machine at the NERSC facility. Approximately 100 ms of physical time was evolved at an effective resolution of 1024^3. An additional 5 ms was evolved at the finest level, generating approximately 6TB of data for detailed analysis. Case M-D was evolved over 64 ms at 1024^3, and an additional 1 ms at 2048^3. This case consumed approximately 1.5M node hours on Franklin and generated approximately 8TB for analysis.

5 Diagnostics and experimental setup

The scalar and velocity fields of the laboratory LSB flame experiments were measured using OH-PLIF and PIV. Details of the OH-PLIF and PIV setups can be found respectively in Cheng et. al. [19] and Johnson et. al. [20]. The OH PLIF system consists of a Spectra Physics pulsed Nd:Yag laser pumping a Quanta Ray dye laser with Rhodamine 590 dye. The output of the dye laser is frequency doubled and tuned to the $P_1(2)$ absorption (282.58 nm) of the OH (1,0) band of the $A^2\Sigma^+$-$X^2\Pi$ system. The laser beam is shaped into a thin (200 nm) vertical sheet passing through the LSB axis. The OH fluorescence signal from the flame is detected by an intensified Xybion camera through band pass filters (Schott UG-5 and WG-305). The camera captures a field-of-view of r = 20 mm and z = 27 mm at a resolution of 60 μm/pixel. For each flame, 400 images are obtained for the analysis.

The PIV system uses a New-Wave Solo Nd:Yag laser with double 120 mJ pulses at 532 nm and a Kodak/Red Lake ES 4.0 digital camera with 2048 by 2048 pixel resolution. The optics was configured to capture a field of view of approximately 13 cm by 13 cm covering the nearfield as well as the farfield of the flames with 0.065 mm/pixel resolution. A cyclone type particle seeder, supplies the air flow with 0.6-0.8 μm Al_2O_3 particles that tracks velocity fluctuations up to 10kHz [21]. For each flame, 224 pairs of PIV images are obtained for velocity statistical analysis. As reported by Peterssen et. al, [5], the asymetry of swirler geometry imposes azimuthal variations in the velocity and the scalars fields. To be consistent with the prior studies, the OH-PLIF and PIV image planes were centered on the only pair of vanes that are aligned with a row of holes on the perforated plate.

The experiments were performed with a $\phi = 0.7$ CH_4/air mixture at six bulk flow velocities,U_0, of 3, 6, 7, 10, 15, and 18 m/s (Table 1). The velocities are higher than those investigated at Lund and Darmstadt to study flowfield development and heat release effects. The turbulence parameters u_z' and u_r' in Table 1, measured on the centerline at the leading edges of the flame brushes according to the procedure of Ref. [3], are the appropriate representations of the initial conditions of these LSB flames. The Reynolds number, Re, Damkholer number, Da, and Karlovitz number, Ka, are also computed as references. The integral length scale for the calculation of Re, Da and Ka was deduced from analysis of the non-reacting flow PIV data reported in Appendix 1. The values of Re, Da, and Ka of all five flames of this study are indicative of flames in the winkled and corrugated flame regimes. As shown in Appendix 1, the non-reacting flowfield only becomes fully developed at $U_0 > 10$ m/s. Therefore, the simulations were performed for the two flames M-C and M-D at $U_0 = 10$ and 15 m/s that are within the fully developed flow regime.

Other parameters listed in Table 1 pertain to the analysis of the flowfields and flame wrinkling processes. They will be described in the next two sections.

6 Flowfield Features

Typical features of the experimental LSB flowfield are shown in Fig. 3 by the 2D velocity vectors for case M-D ($U_0 = 15$ m/s). In the nearfield ($z < 10$ mm) the vectors outline a uniform flow region at the axis ($-10 < r < 10$ mm) flanked by two velocity peaks

(at r = +/- 22 mm) associated with the faster flow through the annular swirling jet. Radial expansion of the swirling jet causes the center region to decelerate with increasing z. The deceleration at the centerline is outlined by contours of the normalized axial velocity, u_z/U_0. A local minimum is reached at $z \approx 22$ mm and $r = 0$. This position corresponds to the leading edge of the flame brush. Downstream of this point, heat release reverses the deceleration trend and generates a slight mean acceleration. In the far field, $z > 70$ mm, the formation of a large but very weak central recirculation zone is outlined by the $u_z = 0$ contour.

Fig. 4 shows the centerline profiles of the normalized mean axial velocity, u_z/U_0, and the normalized 2D turbulent intensity energy q'/U_0. In Fig 4 (a), except for M-A and M-B, the decay of u_z/U_0 in the nearfield ($z < 20$ mm) is linear and similar across a range of flow rates. This self-similar behavior can be quantified by the normalized mean flow divergence rates, a_x, listed in Table 1. Note that the flow acceleration in flame M-A at $15 < z < 35$ mm is disproportionally high. As discussed in Cheng [22], this is caused by the dominance of the flame-generated flow acceleration $\Delta U \approx S_L(T_{ad}/T_0 - 1)$ at small U_0. This condition is labelled "under-developed", and disappears with increasing mean flow rate.

Axial profiles of the scaled turbulent intensity, q'/U_0,, are shown in Fig 4(b). In the near field ($z < 20$ mm), the levels of q'/U_0 for all cases except M-A are the same as expected of turbulence produced by a perforated plate. The q'/U_0 levels within the reactants remain unchanged with increasing z. This non-decaying turbulence is a characteristic of the LSB as reported in previous papers [3]. As listed in Table I, the turbulent intensity produced by the center plate is anisotropic, with the longitudinal fluctuations u_z' about 50% higher than the transverse fluctuations u_r'. In the farfield, the significant increase in q'/U_0 observed for flame M-A ($U_0 = 3$ m/s) is again the consequence of ΔU contributions. Large increases in q'/U_0 are not observed in the farfield when $U_0 > 10$ m/s as the contributions from ΔU become proportionally smaller.

In order to get a sense for the scale and character of the simulated flame solutions, Fig. 5 shows a volume rendering of a snapshot taken from the M-D case, where the

opacity scales linearly with the concentration of the OH molecule. The presence of OH, indicated by the blue cloud, indicates the approximate flame location. The boundary of the computational domain is shown in wireframe, and the cylinder at the bottom was added to show the location and relative size of the LSB nozzle. The overall flame size and shape, as well as the dilution in the shear region at the trailing edges of the flame are consistent with laboratory observation. Note that the fields of view for the experimental diagnostics (20 x 27 mm for OH-PLIF and 13 by 13 cm for PIV) are relatively small compared to the simulation domain. The discussion of the simulated profiles and the experimental data is focused primarily on the central region of the flame where the turbulent flame brush is locally normal to the approach flow.

In order to quantify the mean flame position in the simulation results, we take the temperature field to represent a suitable measure of reaction progress (this strategy is discussed at length in the next section). Conceptually, a three-dimensional steady flame brush profile could be constructed by averaging this progress variable over all time as the flame evolves in response to the turbulent flow structures. In practice however, direct application of the strategy is intractable, due to the immense computing resources that would be required to simulate the system long enough to gather stable statistics. In the present case, we opt to exploit axial symmetry of the mean nozzle profile about the centerline of the burner. Mean profiles are constructed from the 3D solution by transforming the velocity components to polar coordinates, and azimuthally averaging each snapshot of simulation data. The snapshot averages are then averaged over the simulated evolution time.

In Figs. 6 and 7, the normalized 2D velocity vectors from PIV, and the azimuthally averaged results for the LMC simulations are compared for cases M-C and M-D. Contours of the normalized velocity vector magnitude, $|u|/U_0$, are shown in the background. The T = 350K isotherms on the simulated results approximate the leading edges of the flame brush in each case..

The PIV plots on the left sides of Figs. 6 and 7 show that the main difference between the two flames is the formation of a far field center recirculation zone in M-D.

Otherwise, the overall flow pattern, the mean flame position, and the flame shape are similar. The simulated results on the right sides of Figs. 6 and 7 verify that the LMC method captures the salient features of the flame and its flowfield. The prediction of a far field recirculation zone at U_0 = 15 m/s indicates that LMC also captures the evolution of the mean flow.

Discrepancies between the measurements and the simulations are found in the overall flame shapes, minimum flame lift-off height, and the magnitudes of the local velocities. The simulated flames appear to be w-shaped instead of bowl-shaped, and they stabilize at positions considerably farther downstream than in the experiments. In the swirling-flow regions, the magnitudes of the simulated peak velocities are slightly lower than the measurements. In the central nearfield region, the differences between simulations and measurements are shown in Table I by the values of a_z and x_0. The mean flow divergence rates, a_z, of the two simulated nearfield flows are the same but slightly larger than those measured by PIV. The corresponding x_0 show the virtual origins of the simulated flows to be smaller than experiment. This means that the axial decelerations of the simulated flows occur at positions farther downstream than the experiments.

We attribute the observed discrepancies in mean flame statistics to a poor characterization of the inlet velocity specification used for the simulations. As discussed above, the mean inflow for cases M-C and M-D were obtained by scaling the measurements of Ref. [5] at U_0 = 6.2 m/s. This inflow profile is an average of two vertical PIV slices one aligned over the swirl vanes and the other over the vane gaps. Downstream of the vanes, the flow has lower velocity peaks in the swirling region than the flow over the gaps. Averaging these two profiles biases the result towards the lower peak velocities because the areas between the vanes are much larger than the areas over the vanes. In the experimental data shown above, the PIV slice was aligned directly over the vane gaps, and thus captured the higher velocity regions of the swirling jet. PIV measurements with higher peak velocities than the simulations should therefore be expected. The delays in the onset of flow divergence in the simulated flames are also consistent with inlet flow profiles that have peak velocities and swirl number that are much lower than those of the experiment.

The simulations also show a considerable decay of the fluctuation intensity as the flow evolves from the inlet boundary to the leading edge of the flame. This reduces by a considerable amount the small-scale wrinkling of the flame surface, and thus the overall turbulent burning speed of the flames, consistent with our results. Additional numerical tests indicate that the issue here is not one of numerical resolution but rather is a consequence of our procedure for introducing turbulence into our simulation. We simply superimposed decaying turbulence to the mean flow, shaping the inlet intensity to match the measured data. The resulting fluctuations decay rapidly in a way that is not observed in the experiments, suggesting that a better match to experimental data requires a more accurate representation of the turbulent flow leaving the nozzle. The conclusion is consistent with those of Nogenmyer et al., though how to do this in practice remains an open question.

7 Mean and wrinkled flame front structures

The morphology of the experimental flames was inferred from OH-PLIF images, in terms of a mean progress variable, $\bar{c}$, and the 2D local flame curvature κ, as follows. The individual OH-PLIF images were corrected for the non-uniform intensity of the laser sheet as it is attenuated through the flame. An edge-finding algorithm was then used to locate steep gradients in the OH signal to mark the instantaneous flame front positions. These edges were compared manually with the original images in order to remove edges detected in the burnt gas region where the OH intensities eventually drop in the post-flame gas. In fig. 8, examples of the processed flame fronts (red lines) are overlaid on the corresponding PLIF images. Based on the detected flame segments, the OH-PLIF images were binarized, setting regions above the edges to 1 (corresponding to burnt gas) and below the edges to 0 (corresponding to cold fuel). The binarized image sets for each case were then averaged together to produce 2D maps of the mean progress variable $\bar{c}$ in the diagnostic plane. Along the interface between burnt gas and cold fuel, the 2D curvature κ is given by

$$\kappa = \frac{x'y'' - y'x''}{(x'^2 + y'^2)^{3/2}}$$

The sign convention for κ is positive when the center of curvature lies on the products side of the flame, and *(x,y)* are coordinate in the diagnostic plane.

The $\bar{c}$ contours for all five experimental cases are shown in Fig. 9. The flame brush is defined as the region, $0.1 \leq \bar{c} \leq 0.9$. In all case but M-A ($U_0$ = 3 m/s), the leading edge of the flame brush is located near z = 20 mm. The $\bar{c}$ contours also show that when $U_0 \leq$ 10 m/s the brush is asymmetric with respect to the device axis. This is another indication of the developing flowfield at the lower velocities. The flame brush thickness, shown by the distance between the $\bar{c}$=0.10 and 0.90 contours, is approximately 20mm for all cases. Since the values of the fluctuation intensities increase linearly with U_o (see Table I), the flame surface density is expected to increase as well. This is confirmed by the increasing values of the flame length ratio l_f/l_r in Table I. Here, l_f is the mean flame front length obtained from the OH-PLIF images, and l_r is the radial reference length defined by the PLIF field of view.

The PDFs of κ for the five flames and their statistical moments are shown in Fig. 10. All cases show a peak at κ = 0. The increase of their standard deviations with U_0 is consistent with the generation of finer scale wrinkles at higher turbulence levels. The reduction in their skewness with increasing U_0 is also consistent with d

iminishing contributions from kinematic restoration, or flame merging events, in the concave flame segments.

The curvature of the experimental flame surface in the 2D diagnostic plane was characterized further by the conditioned κ PDFs. For each flame, five κ PDFs conditioned on $\bar{c}$ values between 0-0.2, 0.2-0.4, 0.4-0.6, 0.6-0.8 and 0.8-1.0 were deduced. The statistical moments of the conditioned κ PDFs are plotted in Fig 11 as functions of $\bar{c}$. In Fig. 11 (a), the changes in the mean curvatures from positive to negative with increasing $\bar{c}$ simply indicates higher probabilities of encountering positively curved flame fronts at the leading edge, and negatively curved flame fronts at the trailing edge. Standard deviations of the conditioned κ PDFs in Fig. 11 (b) show them to vary with $\bar{c}$ for flames with $U_0 \leq$ 10 m/s. This shows that the kinematic restoration events generating larger negative curvatures at the trailing edge of the flame brush are relevant at lower U_0 with less intense turbulence. The trends of the skewness in Fig. 11 (c) provide more evidence to show that kinematic restoration diminishes at higher U_0.

For the simulation results, flame curvature was extracted from the c = 0.8 iso-surfaces of M-C and M-D where c is a local progress variable defined in terms of

normalized temperature; i.e,, c =$(T-T_u)/(T_b-T_u)$. Note that in this case, the flame contour is a 3D object, and therefore has two principle curvatures, κ_1 and κ_2, at any point. The mean curvature $K = \nabla \cdot \hat{n} = \kappa_1 + \kappa_2$, where $\hat{n}$ is a unit normal on the surface pointing into the products defined by ∇c. We note that the unit normal is well-defined only where the temperature gradient is non-trivial. In each snapshot of the simulation for both cases, K was evaluated near the flame surface and mapped onto the c = 0.8 surface by linear interpolation. Fig. 12 shows the resulting distribution of this quantity, weighted by flame area. In order to more directly approximate the experimental diagnostic, the expression for K was re-evaluated by explicitly zeroing the gradient contribution normal to the interrogation plan, which reduces to the 2D formula. To be consistent with the field of view of the OH-PLIF diagnostic, the simulation was interrogated only for r < 10 mm to compute the pdfs shown in Fig. 12. In Fig. 12 (a) the discrepancy between the simulated and the measured 2D curvatures for case M-C indicates that the simulation is not producing wrinkling at as fine a scale as the experiment. The difference between the simulated 2D and 3D pdfs also implies that the 2D flame curvatures underestimate the degree of three-dimensional flame wrinkling. For case M-D (Fig. 12(b)), the simulated pdfs are broadened compared to M-C, indicating that finer scale wrinkles are generated with increasing turbulent intensity. The discrepancy between the experimental and simulated results is significantly reduced compared to Fig. 12 (a). The results show that the LMC simulations capture the qualitative trend of the flame wrinkling processes. As discussed above, the larger flame wrinkles observed in the simulation data may be associated with errors in experimental characterization of the inlet velocity profiles as discussed above, and as noted earlier reflects a need for a more accurate representation of the turbulent flow evolution from the nozzle.

Local flame analysis

The concept of a "flamelet" [23], is at the root of the basic paradigm for experimental and theoretical premixed flame analysis. The fundamental idea is that for a class of premixed combustion systems, the flame reaction zone is thin with respect to energy-bearing fluid-dynamical length scales, and its internal structure can be expressed in terms of a steady 1D flame idealization. This picture defines a monotonic "reaction progress" indicator to parameterize the flame. Experimental data analysis is based on the

notion that we only need to identify the flame location (using Mie scattering or PLIF data). One then assumes that the local flame structure is given by the idealized 1D flames with possible corrections for steady stretch.

One approach to analyzing the local structure of the simulated LSB flames is to construct a similar type of flamelet representation of the solution by defining a local coordinate system around the flame surface. Such a construction can be made by starting with a tessellation of the flame surface and then extending along integral curves of the gradient of the progress variable as indicated in fig. 13. See [2] for details of this construction. We will refer to diagnostics based on this local coordinate system as "flamelet" diagnostics.

This type of flamelet construction, which presents a flame-centric perspective, can provide useful information about the flame. However, there is a potential problem. For one thing, the fluid element will not, in general, approach the flame along the local flame coordinate. Furthermore, in an unstrained steady ϕ=0.7 CH_4-air flame, a fluid parcel requires approximately 2 ms to move through the preheat zone and to the location of peak OH concentration. This duration is roughly comparable to the eddy "turnover time of 3-4 ms in the LSB experiments. Thus during the time it takes for a fluid parcel on the cold side of the preheat zone to reach the location of peak OH concentration, the conditions can change significantly. So, while our experimental techniques provide a valid representation of the instantaneous flame profiles, there is a clear limitation to how we may interpret them in terms of the classical picture of a "flamelet" even in the rather low levels of turbulence in the LSB configuration.

There are even larger issues in systems with nontrivial transport effects in the preheat zone, such as in lean H_2–air mixtures, where there can be significant fuel transport tangential to the flame isotherm. In those cases, lack of a unique progress measure makes even the identification of a "flame contour" problematic [2]; there is no well-defined quasi-1D model in this case. In either case, care must be exercised when interpreting instantaneous data in terms of the steady flame idealization, particularly when attempting to infer cause-and-effect relationships.

In order to provide an alternative picture of the flame that can capture the inherently transient character of turbulent flame, we extract flowfield and state properties

in a Lagrangian frame by tracking fluid parcels as they move through the reaction front. Such pathlines are constructed from the simulation data by integrating the local velocity field components over a sequence of time intervals defined to span snapshots of the solution that have been written as the simulations proceed. Initial seed points for these paths are chosen in the cold region upstream of the flame, and as the Lagrangian paths are integrated in time various statistics of the solution are collected along the way. The main benefit of this approach is that the dynamic changes within the reacting fronts are incorporated explicitly, allowing us to explore the effects of the time-varying fields. Additionally, the pathline tracing can be applied without ambiguity to interrogate different regions of the CH_4 flame including those where reactions may not be complete, such as near the outer edges of the flame where significant air entrainment and dilution are expected. In the near unity Lewis number case considered here we expect that both the flamelet and pathline types of analysis will yield similar results; however, the pathline technique is expected to be particularly well-suited to investigating the simulated results of H_2 flames as an aid to exploring the changes in local reactivity due to thermal/diffusive effects.

Approximately 7000 Lagrangian pathlines were extracted from a snapshot of the M-C and M-D flame solutions, taken near the central regions (r < 20 mm). Fig 14 shows the pathline trajectories in physical space for case M-D; the set which collectively outlines the divergent nature of the flow. Recall that each path represents a trajectory through space-time; the figure is constructed by ignoring the time coordinate. Close examination reveals that some trajectories have loops and spirals, suggesting a significant interaction with fine scale turbulent structures as the parcels move through the preheat zone. The typical length of these pathlines is on the order of 10 mm, which represents the convective distance the particles move as they react from cold fuel to burned products. Properties extracted on the pathlines include temperature, velocity components, species concentrations, and chemical production rates. We also compute local mean curvature , K, Gaussian curvature, $G = \kappa_1 \kappa_2$, and the tangential strain rate (or, divergence of the flow in the progress contours) along the pathline.

Fig. 15 shows the scatter plots of strain rate versus curvature conditioned at c = 0.8 where CH_4 consumption rate reaches its maximum in the solution of a 1D unstretched

laminar CH_4/air flame at $\phi = 0.7$. Fig 15 (b) shows that the increase in turbulence intensity in flame M-D results in more scatter.

The Gaussian and mean curvatures together describes the local topology of the flame wrinkles. Positive G indicates that the burning occurs in "spherical" regions and negative G indicates "saddle" regions. The cross-correlation of Gaussian and mean curvatures at c = 0.8 are shown in Fig. 16. These plots allows us to differentiate pathlines that traverse flames fronts that are locally convex ($G > 0$, $K > 0$), concave ($G > 0$, $K < 0$), cylindrical ($G = 0$) or saddle ($G < 0$) to the reactants. Fig. 16 (a) shows that the flame elements of M-C are mostly cylindrical and cluster on the $G = 0$ axis. The smallest wrinkles have spherical geometry and are concave to the reactants ($G > 0$, $K < -1000$). However, there are no corresponding small scale convex flame wrinkles. For M-D (Fig. 16 (b)), there are increased probabilities of flame wrinkles having saddle, concave and convex geometries due to the increase in turbulence. But the skewness toward negative curvatures remains.

Although the flames show significant stretch effects, the near unity Lewis number implies that the local flame propagation speed should be nearly constant. We can integrate the fuel consumption rate over each tubular element (depicted in Fig. 13) in the flamelet representation to compute a local consumption flame speed. A PDF of these local speeds for M-C and M-D are presented in fig. 17. As expected, we see little variation in the distributions. In both case, the mean value is consistent with the laminar burning speed, and the distribution around the mean is symmetric, and weakly dependent on turbulence level.

Fig. 18 compares temperature profiles on selected pathlines (a) and selected flamelets (b) through concave, convex, flat ($G = 0$, $M = 0$) and saddle flame geometries. The pathline profiles are plotted versus a relative time, *t*, with *t=0* at the time when the particle on a pathline reaches a temperature of 1550K (i.e. c = 0.8). The flamelet profiles are plotted versus distance along the integral curve from the 1550K isotherm. For reference, the temperature profile is shown from the corresponding steady unstretched 1D solution. We note that the acceleration through the flame leads to a nonlinear relationship between the time scale for pathlines and the spatial scale for the flamelets

For M-C at U_0 = 10 m/s, the profiles at temperatures above 1500K closely follow the unstrained 1D laminar flame profile for both pathlines and flamelets. The largest differences are found in the preheat zone below 1500K. For the pathlines through concave flame geometry, temperatures are slightly below that of the 1D flame. The pathlines though flat and convex flame geometries show earlier heating, most pronounced in the convex pathlines. For the flamelets, we also see variation in the preheat zone but it does not appear to correlate with curvature measures, indicating the role of transient behavior in the dynamics. For M-D at U_0 = 15 m/s, deviations from the 1D profile are found in the preheat zone and also the heat release zone above T = 1500K. Close examination shows that the temperature profile of the pathlines through saddle flame geometry most closely match the 1D profile. The temperature gradients of pathlines through concave geometry are generally steeper than those of the 1D profile. The gradients are also steeper than those of their counterparts in M-C due higher negative curvature. Conversely, M-D pathlines through regions of convex flame geometry with large positive curvature show more preheating compared to those of M-C. Again in the flamelet representation the distribution in the preheat zone does not appear to correlate with flame geometry.

Fig. 19 shows the flame front structures in terms of OH concentration and CH_4 consumption rate. For both cases, the OH profiles closely follow that of the 1D laminar flame at c > 0.8 with no apparent dependency on the local flame geometry. At c < 0.8, the OH concentrations from both flames are slightly higher than the 1D laminar flame but their trends are consistent. The main difference between the two cases is an increase in the data scatter due to higher turbulence of M-D. The OH profiles versus progress variable appear to be insensitive to which representation is selected.

The dynamic nature of the flame fronts are shown on the profiles of curvature and strain rates in Fig. 20. For the curvatures, the tendency of the profiles to band together at c = 0.8 is due to the use of the curvatures as the conditional parameter to identify the local flame geometry. In both flames, the curvatures through flat and saddle flame geometries remain unchanged and close to zero. Increasing trends are shown on the pathlines traversing concave and convex flame geometries. The pathlines through convex flame geometry have curvature values near zero at c = 0 that increase through the

reaction zones. The profiles for the concave geometry all have negative curvature values at $c = 0$ that evolve to lower curvatures through the reaction zone.

For M-C, the strain rate profiles show that the pathlines through the convex and flat flame geometries are small and remain relatively unchanged through the reaction zones. The profiles through concave flame geometries show a different trend with the strain rates increasing from near zero at $c = 0$ to higher values at $0.2 < c < 0.8$ then decreasing to near zero at $c \approx 1$. In comparison, much more scatter is shown on the strain rate profiles for M-D. Close examination shows that increased turbulence causes rapid changes in the strain rates on the pathlines through flat, saddle and convex flame geometries. The evolution of the strain rates through concave flame geometry is similar to the trend shown by M-C. These diagnostics show that the fluid parcels experience large and rapidly changing stretch as they pass through the flame zone. Strain rates locally exceed the extinction strain rate [24]; however, we see no evidence that the flame is being affected appreciably in these cases.

Conclusion

Our experimental and numerical investigation of premixed turbulent CH_4/air flames generated by a low-swirl burner shows that the LMC simulations captured the salient features of the flame, the flame stabilization mechanism and the evolution of the flowfield with U_0. The 3D time-dependent simulations allow us to follow the complex interaction of the flame and the turbulence in considerable detail.

The experiments were performed at a velocity range of $3 < U_0 < 18$ m/s to characterize this benchmark LSB. The results show that the flowfield of this LSB is not fully developed for $U_0 < 10$ m/s. Therefore, the simulations were performed at U_0 of 10 and 15 m/s to avoid the conditions where rapid changes may occur. Comparison of the measured and simulated flowfield parameter and flame front properties is satisfactory. The use of averaged experimental profiles to specify inflow boundary conditions for the simulations has some serious drawbacks, and this may be the main source of discrepancy between the measured and the simulated results. Nevertheless, the comparisons demonstrate that the simulations capture the overall dynamic behaviors of the flame and the turbulent flow fields, and are therefore relevant for more in depth probing. In particular, it may be interesting to interrogate different regions of the burner flow, such as

where combustion has been diluted by mixing with air on the periphery of the flow, and to quantify the extent and features of unburned fuel pockets downstream of the central flame region.

The comparisons presented here suggest several improvements to the simulation procedure. First, we need to obtain boundary data that is more representative of the fully developed nozzle flow. This would include the axial variation in the mean profiles and a better characterization of the turbulence leaving the nozzle. Our strategy will be to combine simulation of flow within the nozzle with more detailed nonreacting flow experiments to obtain improved data.

We have considered two paradigms for analysis of the local flame structure. One is based on a traditional static flamelet construction. The other is based on the use of Lagrangian pathlines. We showed that, as expected for near unity Lew number flames, the results were relatively insensitive to the choice of diagnostic approach. For low Lewis number flames, to be discussed in future work, the different approaches provide different insights into the flame behavior. The pathlines used here for analysis were obtained in a postprocessing step from field data. For the diagnostic presented here that was effective; however, for more rapidly changing fields, this approach led to a poor characterization because the sampling was too sparse. We plan to add the capability to the simulation code to collect this data as the simulation runs. This will enable us to not only collect more, higher-quality data but will also reduce the overall computational costs of obtaining the data.

Acknowledgement

This work was supported under the DOE SciDAC Program by US Department of Energy under Contract No. DE-AC02-05CH11231. The simulations and analysis were performed on the Franklin and Hopper machines at NERSC under an INCITE award. The authors gratefully acknowledge Gary Hubbard in the LBNL Combustion Laboratory for assistance in data analysis, and Mathieu Legrand Department of Thermal and Fluids Engineering, Universidad Carlos III, Madrid, Spain, for detailed imaging of the LSB nozzle flows that helped illuminate deficiencies in the mean flow specifications for the simulation boundary conditions.

References

[1] J. B. Bell, R. K. Cheng, M. S. Day and I. G. Shepherd, Proceedings of the Combustion Institute, 31 (1) (2007) 1309-1317.

[2] M. Day, J. Bell, P.-T. Bremer, V. Pascucci, V. Beckner and M. Lijewski, Combustion and Flame, 156 (5) (2009) 1035-1045.

[3] B. Bedat and R. K. Cheng, Combustion and Flame, 100 (3) (1995) 485-494.

[4] R. K. Cheng, D. T. Yegian, M. M. Miyasato, G. S. Samuelsen, R. Pellizzari, P. Loftus and C. Benson, Proc. Comb. Inst., 28 ((2000) 1305-1313.

[5] P. Petersson, J. Olofsson, C. Brackman, H. Seyfried, J. Zetterberg, M. Richter, M. Aldén, M. A. Linne, R. K. Cheng, A. Nauert, D. Geyer and A. Dreizler, Applied Optics, 46 (19) (2007) 3928-3936.

[6] J. B. Bell, M. S. Day, I. G. Shepherd, M. R. Johnson, R. K. Cheng, J. F. Grcar, V. E. Beckner and M. J. Lijewski, Proc. Natl. Academy Sci. USA, 102 (29) (2005) 10006-10011.

[7] J. B. Bell, M. S. Day, J. F. Grcar, M. J. Lijewski, J. F. Driscoll and S. A. Filatyev, Proceedings of the Combustion Institute, 31 (1) (2007) 1299-1307.

[8] R. K. Cheng and I. G. Shepherd, Combustion and Flame, 85 (1-2) (1991) 7-26.

[9] R. K. Cheng, D. Littlejohn, P. Strakey and T. Sidwell, Proc. Comb. Inst., 32 ((2009) 3001-3009.

[10] M. S. Day, J. B. Bell, J. F. Grcar and M. J. Lijewski, Proc. ECCOMAS-CFD, 2006,

[11] M. S. Day and J. B. Bell, Combustion Theory and Modelling, 4 (4) (2000) 535 - 556.

[12] R. G. Rehm and H. R. Baum, J. of Reserach of the National Bureay of Standards, 83 (3) (1978) 397-308.

[13] A. Majda and J. Sethian, Combustion Science and Technology, 42 (3) (1985) 185 - 205.

[14] A. S. Almgren, J. B. Bell and W. G. Szymczak, SIAM Journal on Scientific Computing, 17 (2) (1996) 358-369.

[15] K.-J. Nogenmyr, P. Petersson, X. S. Bai, A. Nauert, J. Olofsson, C. Brackman, H. Seyfried, J. Zetterberg, Z. S. Li, M. Richter, A. Dreizler, M. Linne and M. Aldén, Proceedings of the Combustion Institute, 31 (1) (2007) 1467-1475.

[16] K.-J. Nogenmyr, X. S. Bai, C. Fureby, P. Petersson, R. Collin, M. Linne and M. Aldén, AIAA Aerospace Sciences Meeting, AIAA, Reno, Nevada, 2008,

[17] K.-J. Nogenmyr, C. Fureby, X. S. Bai, P. Petersson, R. Collin and M. Linne, Combustion and Flame, 156 (1) (2009) 25-36.

[18] G. I. Taylor, Proceedings of the Royal Society of London. Series A - Mathematical and Physical Sciences 164 (919) (1938) 476-490

[19] R. K. Cheng, I. G. Shepherd, B. Bedat and L. Talbot, Combustion Science and Technology, 174 (1) (2002) 29-59.

[20] M. R. Johnson and R. K. Cheng, 19th International Colloquium on the Dynamics of Explosion and Reactive Systems, Hakone, Japan, 2003,

[21] A. Mellings, Measurements Sci. & Tech., 8 ((1997) 1406-1416.

[22] R. K. Cheng, Combustion and Flame, 101 (1-2) (1995) 1-14.

[23] N. Peters, Combustion Science and Technology, 30 (1) (1983) 1 - 17.

[24] C. K. Law, C. J. Sung, G. Yu and R. L. Axelbaum, Combustion and Flame, 98 (1-2) (1994) 139-154.

Appendix - Characterization of the LSB flowfield and self-similarity

Fig. A-1 shows the normalized two-component velocity vectors of the non-reacting flows at U_0 = 3, 10 and 18 m/s. These vector plots show typical features of the non-reacting LSB flowfield with a central low velocity region surrounded by faster swirling flows through the vane annulus. The evolution of the flowfield downstream is shown by the color contours of the normalized axial velocity, u_z/U_0. The data indicates an upstream shift of the central low velocity region with increasing U_0. The developing nature of the non-reacting flowfield is shown more clearly by the centerline profiles of u_z/U_0 for the five non-reacting flows (Fig A-2). For all cases, u_z/U_0 decays linearly with increasing z to near zero before recovering further downstream. Shifting of the minimum u_z/U_0 positions occurs for all U_0 < 10 m/s. Note that the 15 and 18 m/s cases are self-similar in this normalization. Two parameters can be deduced from centerline u_z/U_0 profiles: the normalized axial stretch rate, a_x, and the virtual origins. These can be used to characterize the nearfield profiles of the mean axial flow. Their values for the U_0 > 10 m/s cases (Table A1) are typical of those of the other LSBs.

Table A1

U_0 (m/s)	x_0 (mm)	a_x (mm^{-1})
3	-48.4	-0.0075
6	-58.9	-0.008
10	-69.74	-0.0076
15	-81.4	-0.007
18	-81.4	-0.007

The centerline u_z/U_0 profiles obtained at LBNL and at Lund for the non-reacting and reacting LSF-1 (U_0 = 6.2, ϕ = 0 and 0.62 [5]) are compared in Fig. A-3. The non-reacting flows produced by the two burners are consistent for z < 20 mm, with slight differences apparent further downstream. Notably, for LSF-1 the Lund burner generated flow recirculation and LBNL burner did not. It is interesting to note that LSF-2 in Ref [5] at U_0 = 9.2 m/s did not generate a downstream recirculation zone. This difference is significant, and is perhaps due to details of the swirler fabrication. From a practical standpoint, it is desirable to operate the LSB nozzle in self-similar conditions. Consequently, we selected the conditions of our numerical studies to be above U_0 =10 m/s to avoid the flow transition regime shown here.

The above characterization of the nearfield flows is based on a simplified picture that LSB swirler generates an azimuthally symmetric flow field. However, due to the geometry of the vane hardware and the perforated turbulence plate, the nozzle in fact exhibits considerable axial variation. PIV data from the Lund group obtained on horizontal cuts above the burner showed a clear "imprint" of the nozzle hardware—an axially periodic variation of mean flows consistent with the geometry of the swirler vane layout. As a result of this variation, measured mean profiles are a strong function of the orientation of the diagnostic plane with respect to the vane geometry. Moreover, the hexagonal-radial pattern of holes in the perforated plate interacts with the 8-fold symmetry of the vanes. To be consistent with the Lund measurements, our axial PIV

measurements were gathered by aligning one of the 4 pairs of opposing vanes to a row of holes distributed radially on the perforated plate. Fig. A-4 shows that the radial profiles of u_z/U_0 at z = 10 mm for the reacting and non-reacting flows of LSF-1 from Lund and from LBNL are consistent. The only observable difference is the peak values of u_z/U_0 on the left

Figure Captions:

Fig. 1 Lifted flame of the low-swirl burner.

Fig. 2 (a) Cross-sectional view of the LSB and (b) its swirler.

Fig 3 Mean 2D velocity vectors measured in a CH_4/air flame of ϕ= 0.7 and U_0 = 15 m/s (case M-D).

Fig 4 Centerline profiles of mean axial velocity (upper) and fluctuations (lower) for CH_4/air flames of ϕ= 0.7 and U_0 = 3, 6, 10, 15 and 18 m/s.

Fig 5 Volume rendering of instantaneous OH concentration for case M-D (U_0 = 10 m/s). The cylinder indicates the location of the applied inlet flow; the green ribbon was added to suggest the general nature of the mean swirling flow entering the domain from the nozzle.

Fig. 6 Measured and simulated 2D normalized mean velocity vectors for case M-C at U_0 = 10 m/s. (same legend as in Fig. 3)

Fig. 7 Measured and simulated 2D normalized mean velocity vectors for case M-D at U_0 = 15 m/s. (same legend as in Figure 3)

Fig. 8 Examples of the OH-PLIF images and the detected flame fronts (in red).

Fig. 9 From left to right, $\bar{c}$ contours of the central regions of flames M-A, M-B, M-C M-D, and M-E deduced from OH-PLIF.

Fig. 10. Experimental unconditioned pdfs of 2D flame curvature (left) and their moments (right).

Fig. 11. Statistical moments of the experimental conditioned pdfs of 2D flame front curvatures from experiments

Fig 12. Experimental 2D flame curvatures, and simulated 2D and 3D flame curvatures for cases M-C (upper) and M-D (lower).

Fig 13 Local coordinate system based on tessellation of the flame surface. A tubular flame element passes through the surface.

Fig 14 Pathlines extracted from simulated flame M-D at U_0 = 15 m/s.

Fig. 15 Scatter plots of conditioned (at c = 0.8) curvature and strain rate from simulations of M-C and M-D.

Fig 16 Scatter plots of Gaussian curvature and mean curvature for M-C and M-D.

Fig 17 PDFs of local consumption flame speed, S_c, for case M-C and M-D.

Fig 18 Temperature profiles on randomly selected pathlines (top) and flamelets (bottom) for M-C (left) and M-D (right).

Fig 19. X[OH] as a function of progress variable on randomly selected the pathlines (top) and flamelets (bottom) representing cases M-C (left) and M-D (right).

Fig 20 Curvature (top) and strain rate (bottom) along pathlines for case M-C and M-D.

Fig A-1 2D normalized velocity vectors of the non-reacting flows generated by the LSB at U_0 = 3, 10, and 18 m/s.

Fig A-2 Centerline normalized axial velocity profiles of the LBNL LSB non-reacting flows at U_0 = 3, 6, 10, 15 and 18 m/s corresponding to flames M-A to M-E.

Fig A-3 Comparison of the centerline axial velocity profiles obtained at Lund and at LBNL.

Fig A-4 Comparison of the radial profiles of the axial velocity (at z = 10 mm) obtained at Lund and at LBNL.

Table I – Conditions of the experimental and simulated ϕ = 0.7 CH_4/air flames

		Measured									Simulated	
Case	**U_0 m/s**	**u_z' m/s**	**$u_{r'}$ m/s**	**u_z'/S_L**	**Re**	**Da**	**Ka**	**a_x 1/mm**	**x_0 mm**	**l_f/l_r**	**a_x 1/mm**	**x_0 mm**
M-A	3	0.4	0.22	2	77	15	0.47	-0.009	-53.4	1.7		
M-B	6	0.49	0.27	2.5	94	12	0.64	-0.0129	-40.4	2.1		
M-C	10	0.62	0.43	3.2	119	9.7	0.92	-0.0116	-49.5	2.41	-0.0177	-15.9
M-D	15	0.85	0.57	4.3	163	7.1	1.47	-0.0119	-50.0	2.65	-0.0176	-16.1
M-E	18	1.15	0.68	5.9	221	5.3	2.3	-0.0127	-46.3	2.8		

Figure 1. Lifted flame of the low-swirl burner.

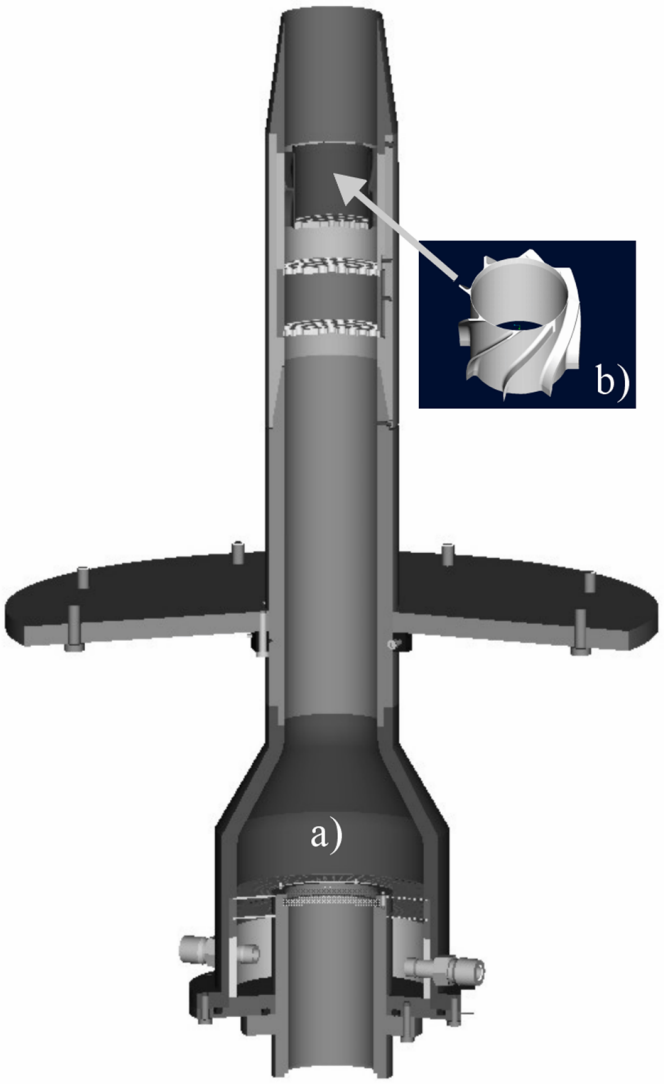

Figure 2. (a) Cross-sectional view of the LSB and (b) its swirler.

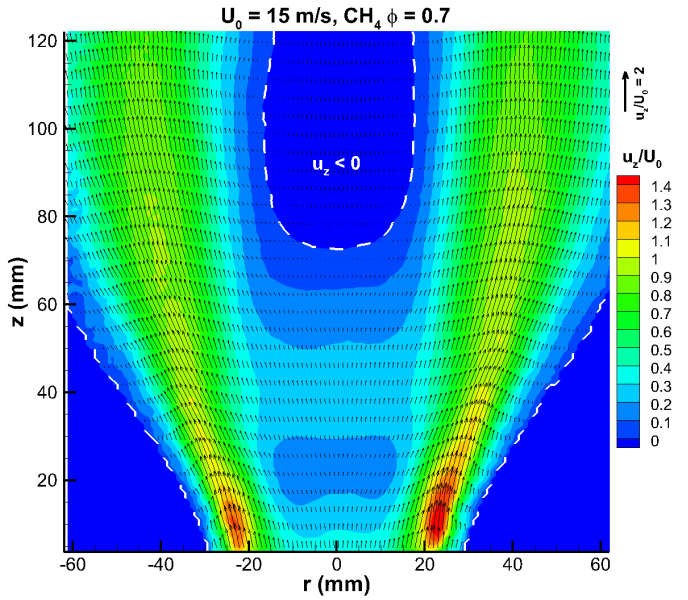

Figure 3. Mean 2D velocity vectors measured in a CH4/air flame of $\phi = 0.7$ and $U_0 = 15$ m/s (case M-D).

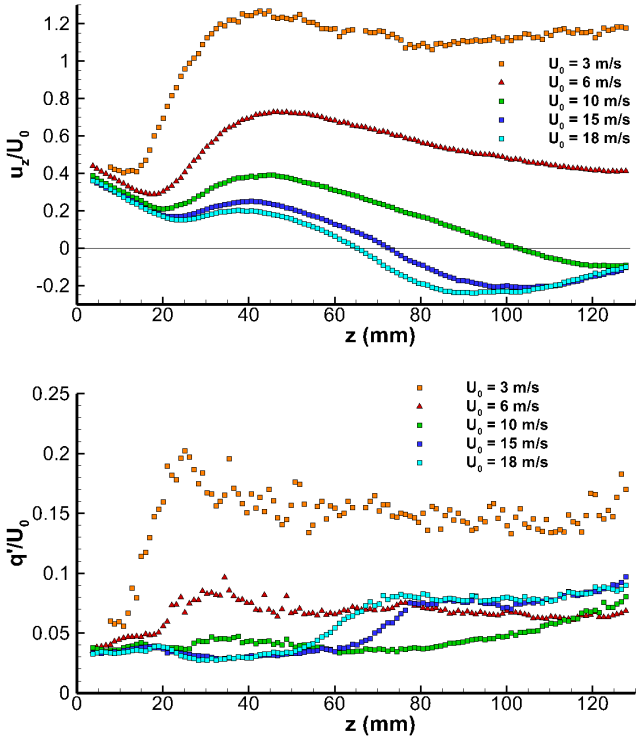

Figure 4. Centerline profiles of mean axial velocity (upper) and fluctuations (lower) for CH4/air flames of $\phi = 0.7$ and $U_0 = 3$, 6, 10, 15 and 18 m/s.

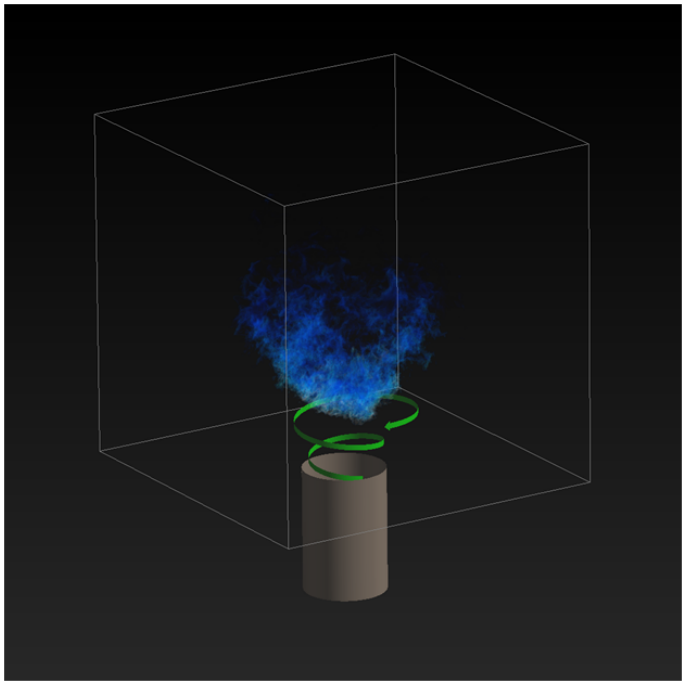

Figure 5. Volume rendering of instantaneous OH concentration for case M-D (U_0 = 10 m/s). The cylinder indicates the location of the applied inlet flow; the green ribbon was added to suggest the general nature of the mean swirling flow entering the domain from the nozzle.

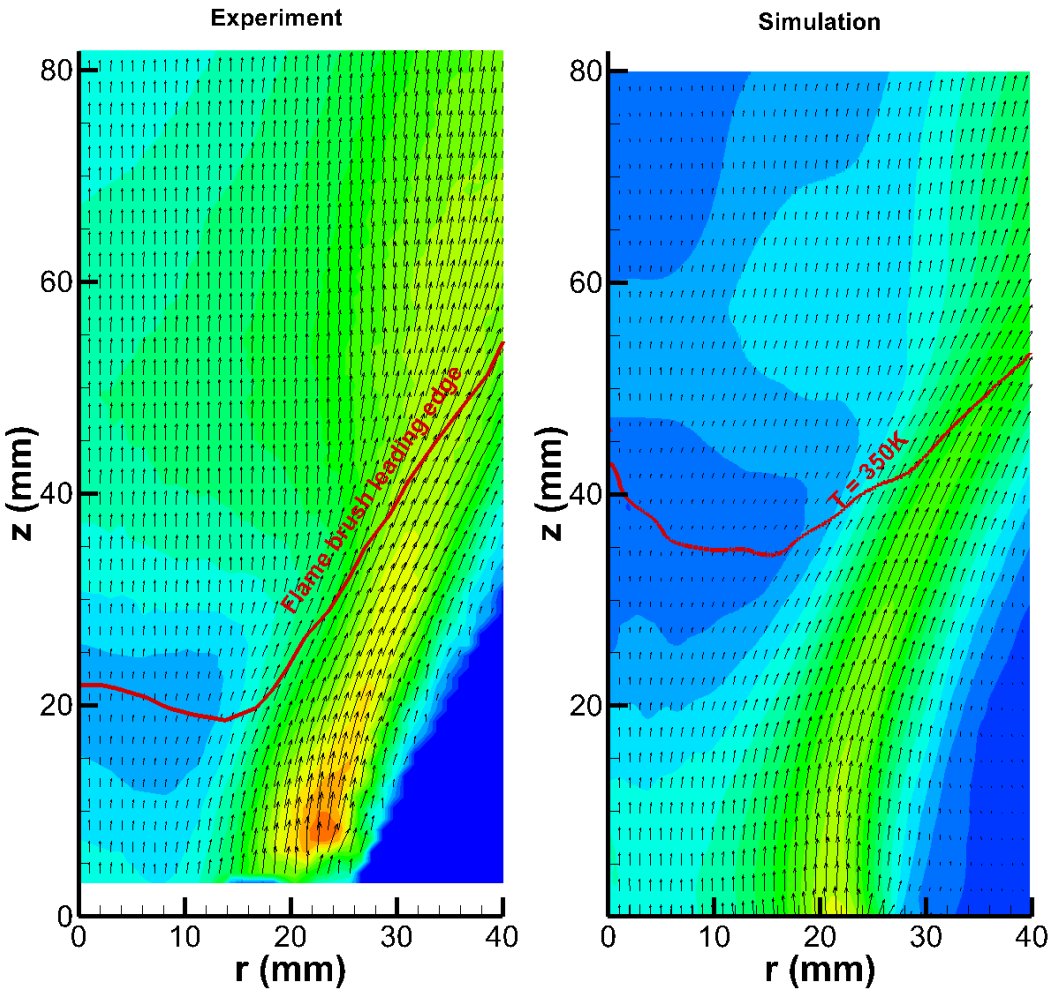

Figure 6. Measured and simulated 2D normalized mean velocity vectors for case M-C at $U_0 = 10$ m/s. (same legend as in Fig. 3)

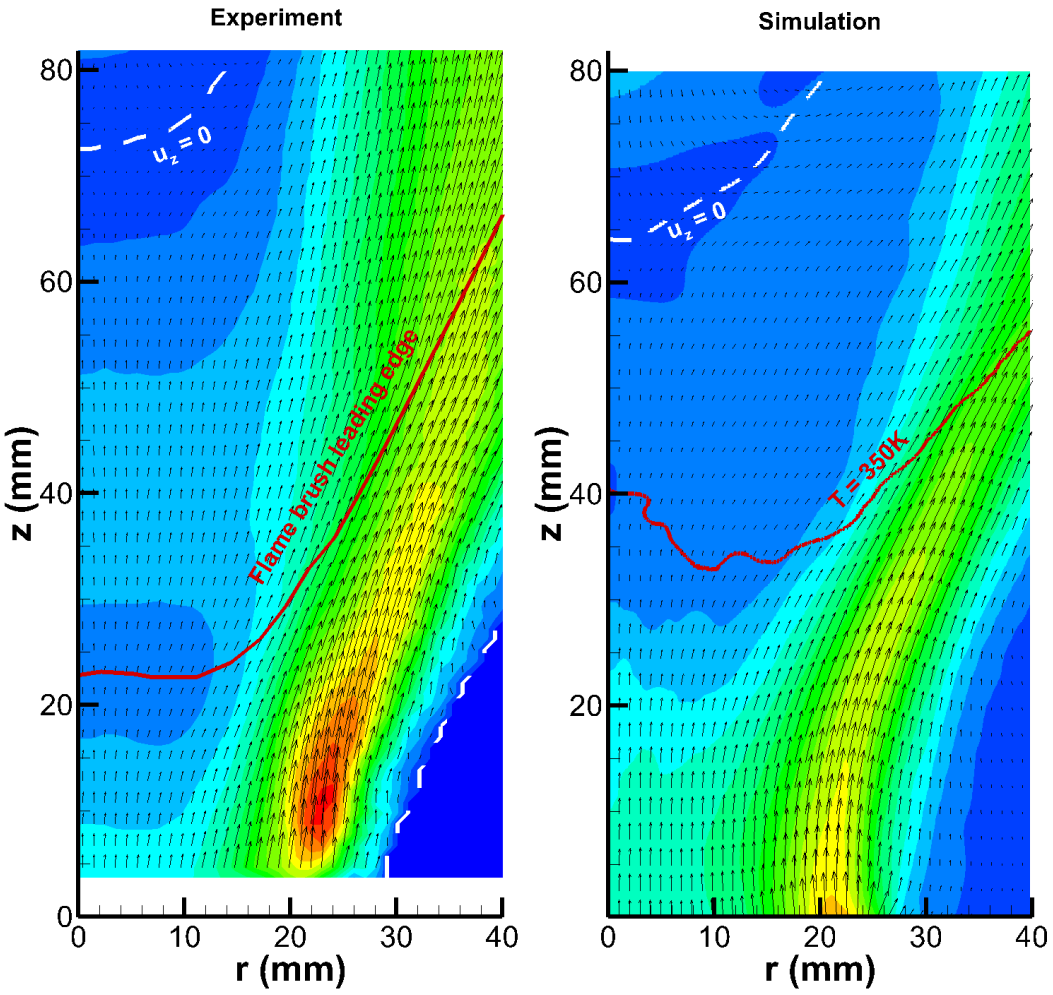

Figure 7. Measured and simulated 2D normalized mean velocity vectors for case M-D at $U_0 = 15$ m/s. (same legend as in Figure 3).

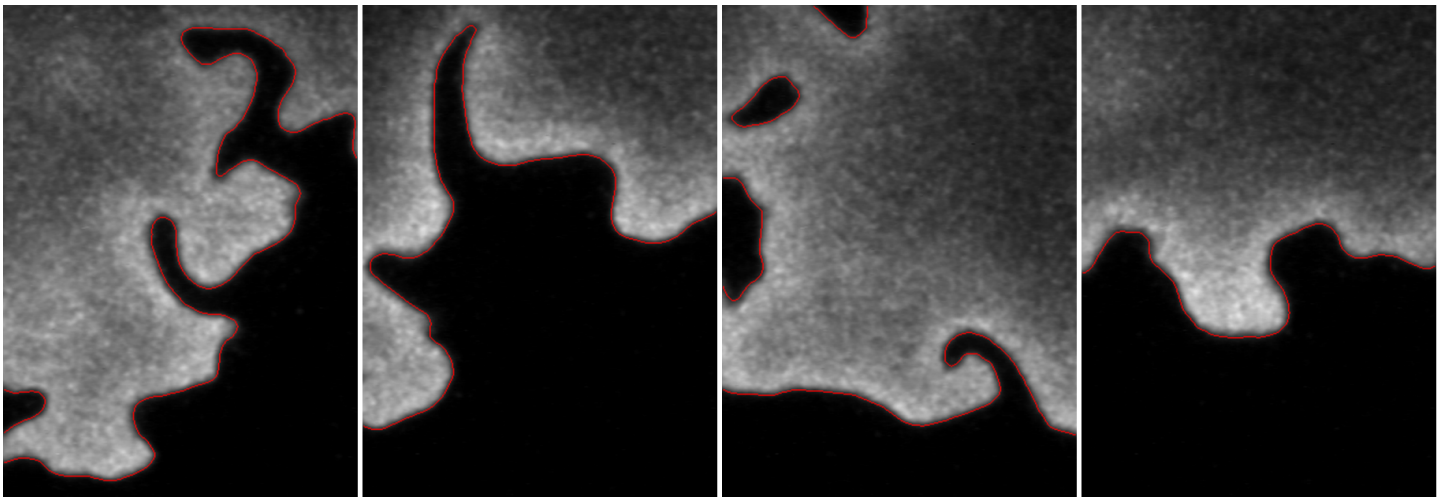

Figure 8. Examples of the OH-PLIF images and the detected flame fronts (in red).

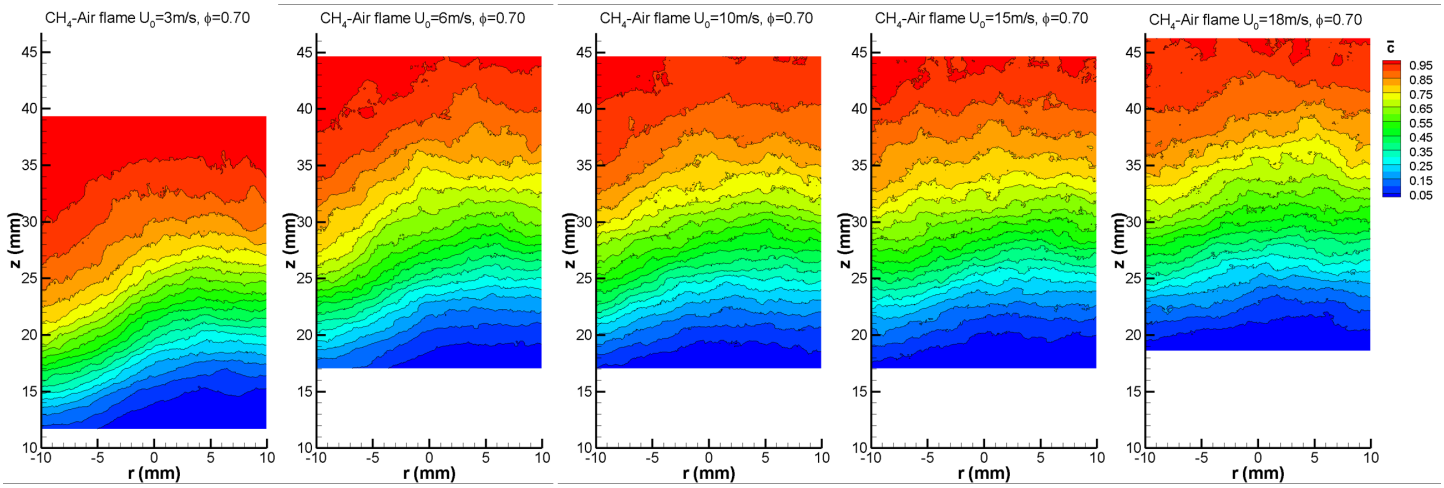

Figure 9. From left to right, $\bar{c}$ contours of the central regions of flames M-A, M-B, M-C M-D, and M-E deduced from OH-PLIF.

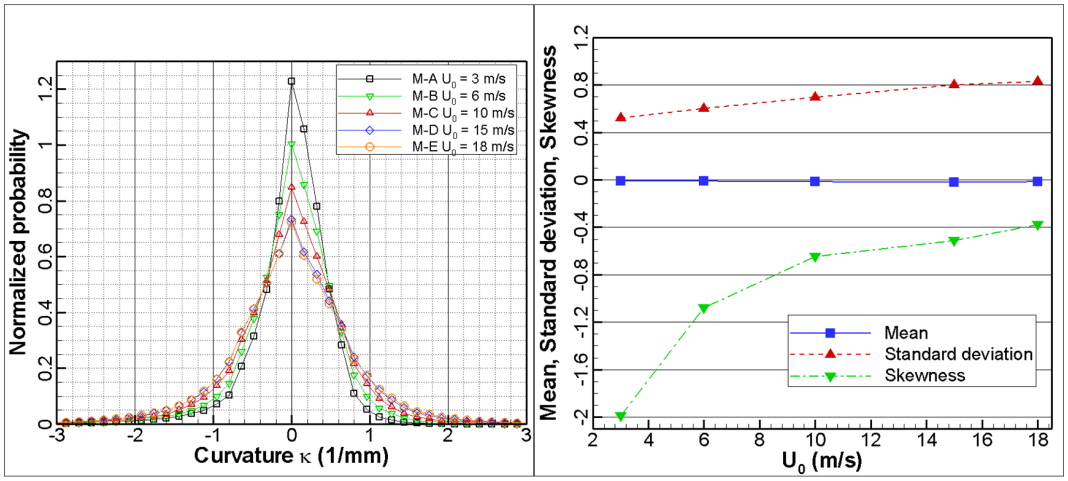

Figure 10. Experimental unconditioned pdfs of 2D flame curvature (left) and their moments (right).

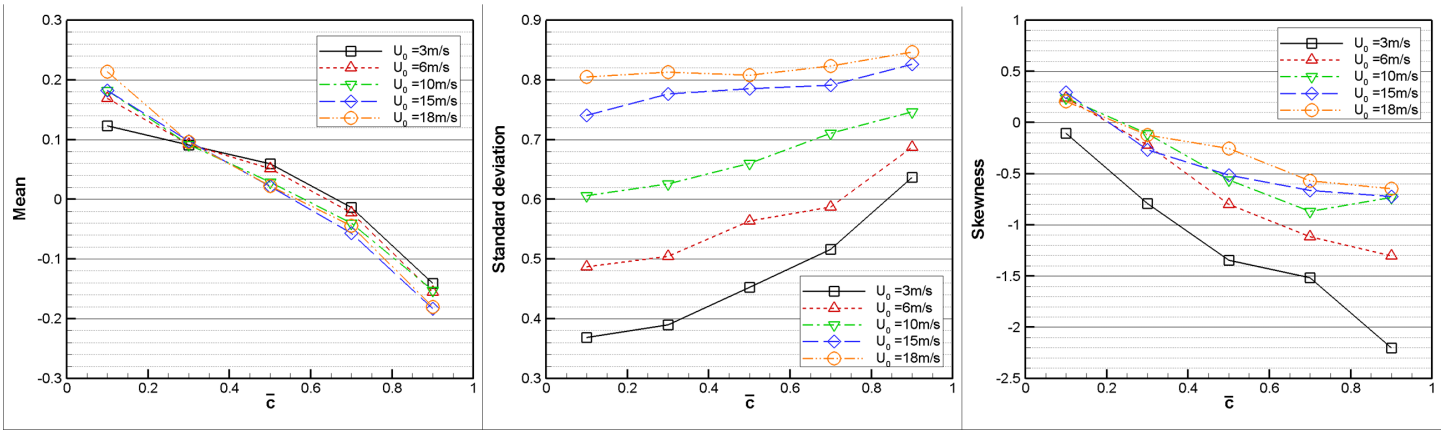

Figure 11. Statistical moments of the experimental conditioned pdfs of 2D flame front curvatures from experiments.

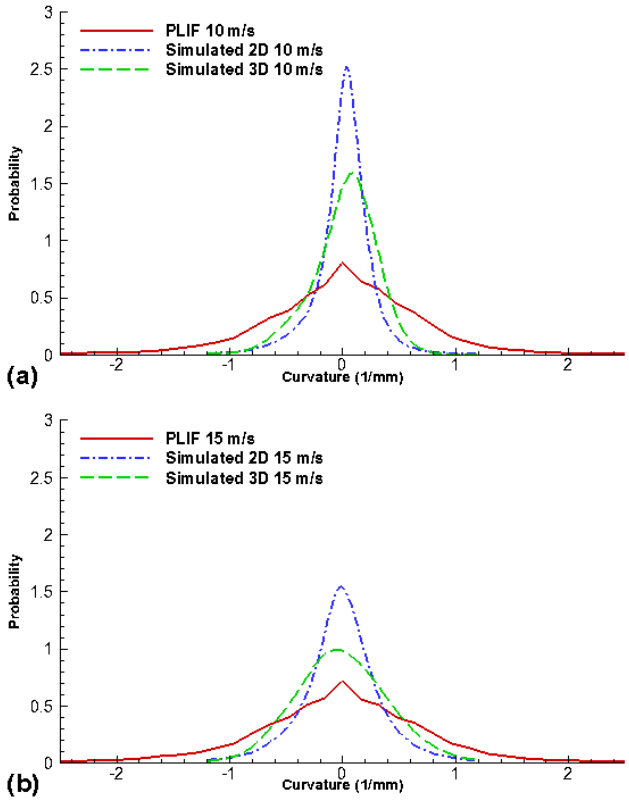

Figure 12. Experimental 2D flame curvatures, and simulated 2D and 3D flame curvatures for cases M-C (upper) and M-D (lower).

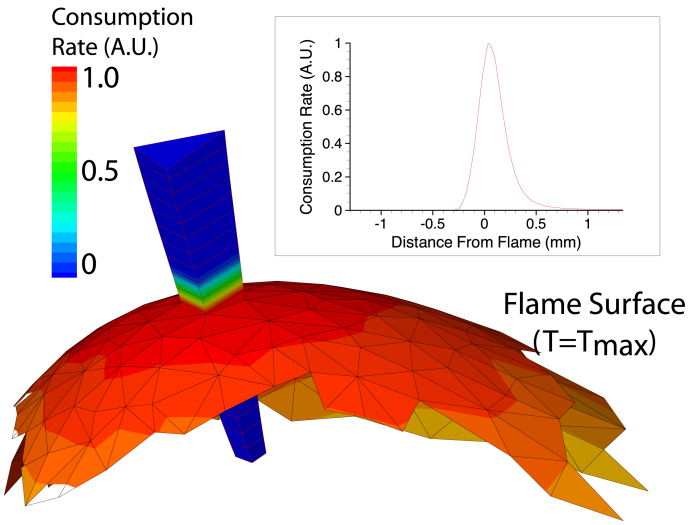

Figure 13. Local coordinate system based on tessellation of the flame surface. A tubular flame element passes through the surface.

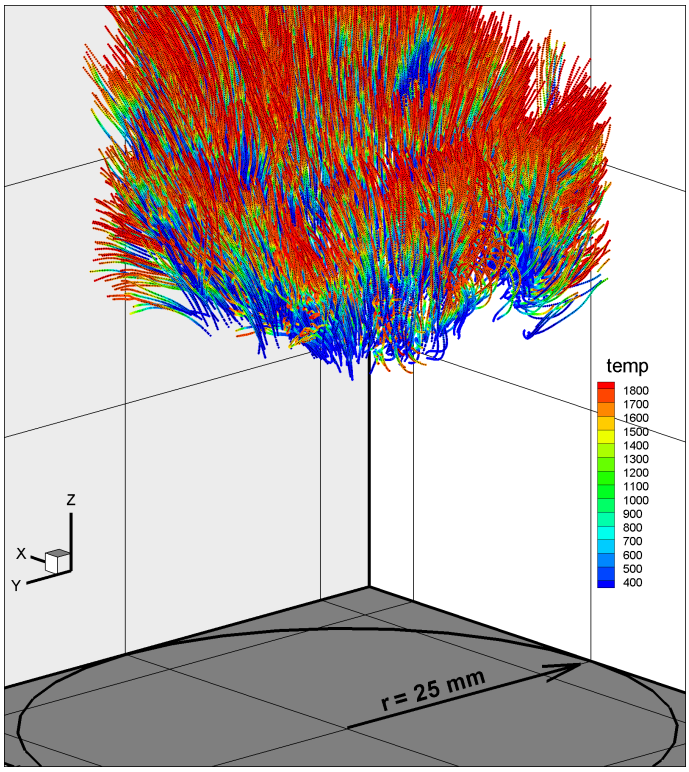

Figure 14. Pathlines extracted from simulated flame M-D at $U_0 = 15$ m/s.

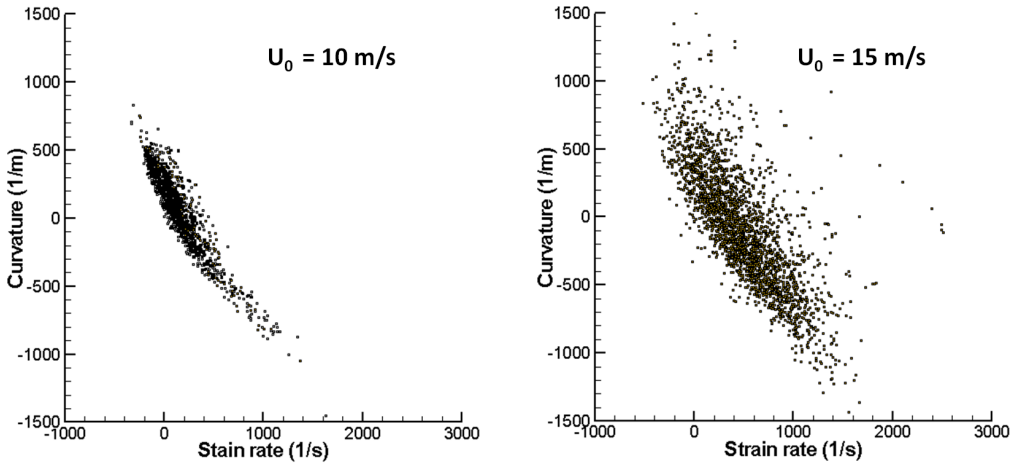

Figure 15. Scatter plots of conditioned (at $c = 0.8$) curvature and strain rate from simulations of M-C and M-D.

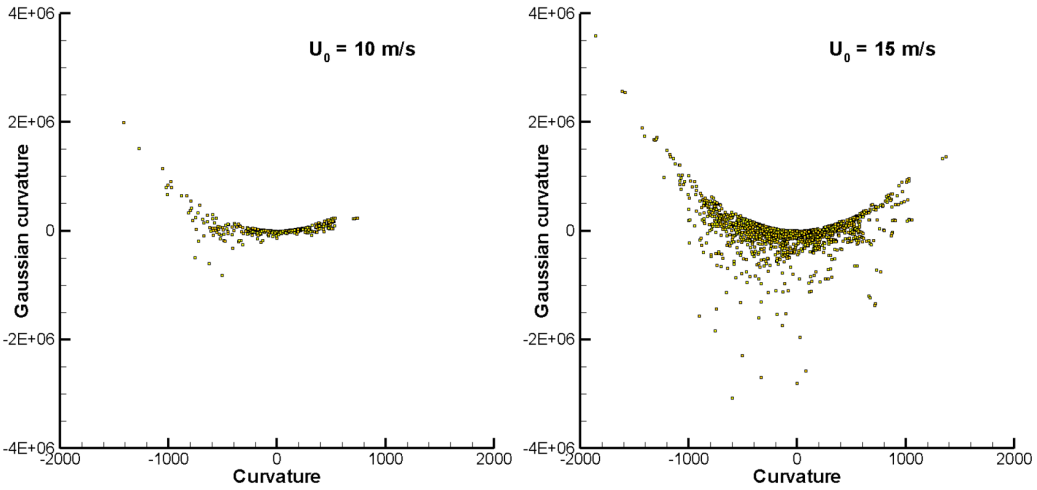

Figure 16. Scatter plots of Gaussian curvature and mean curvature for M-C and M-D.

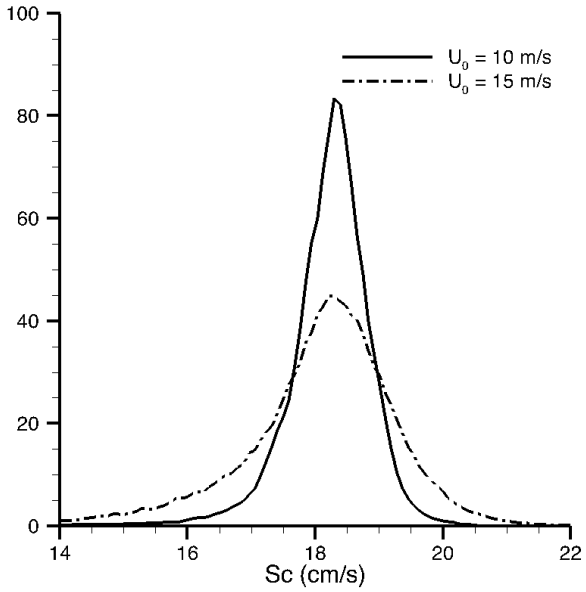

Figure 17. PDFs of local consumption flame speed, S_c, for case M-C and M-D.

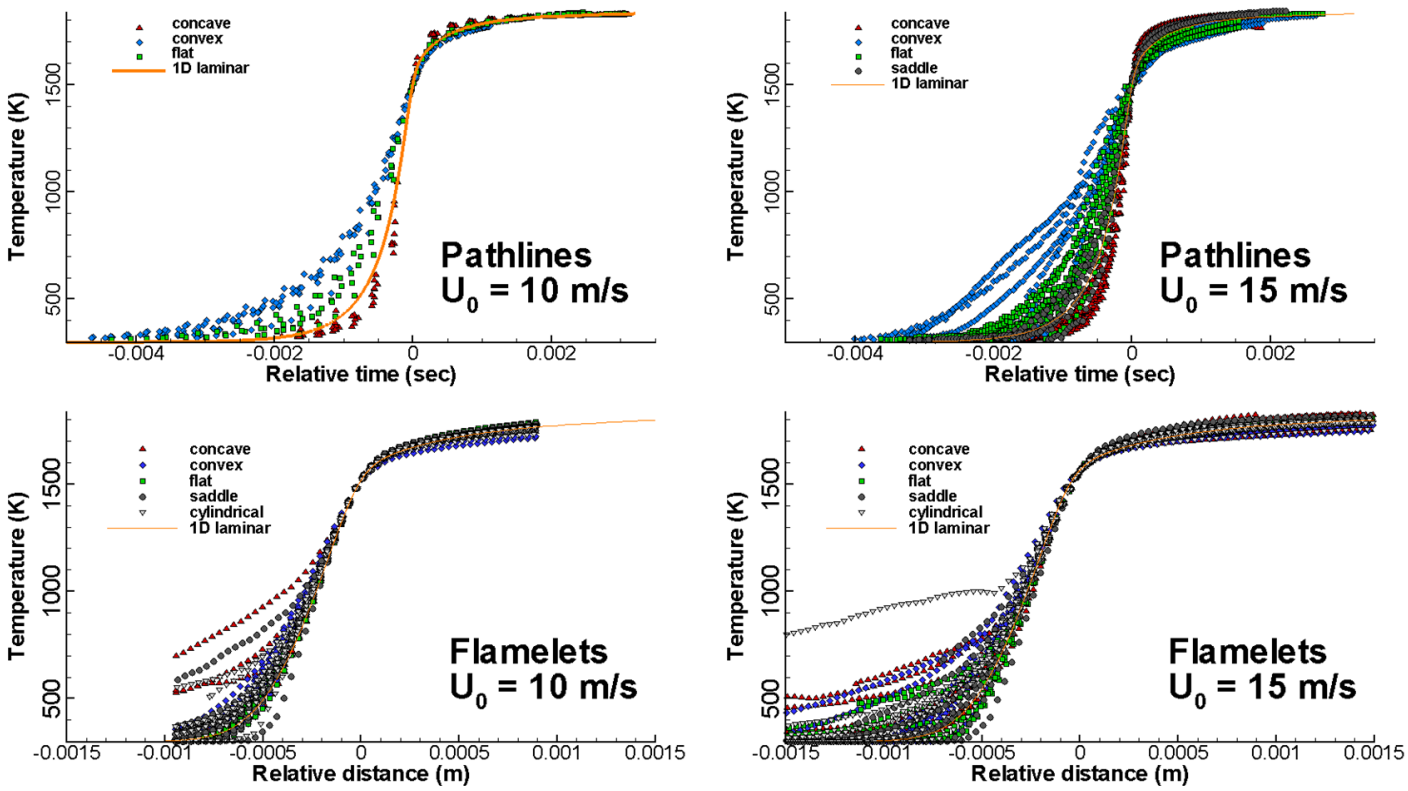

Figure 18. Temperature profiles on randomly selected pathlines (top) and flamelets (bottom) for M-C (left) and M-D (right).

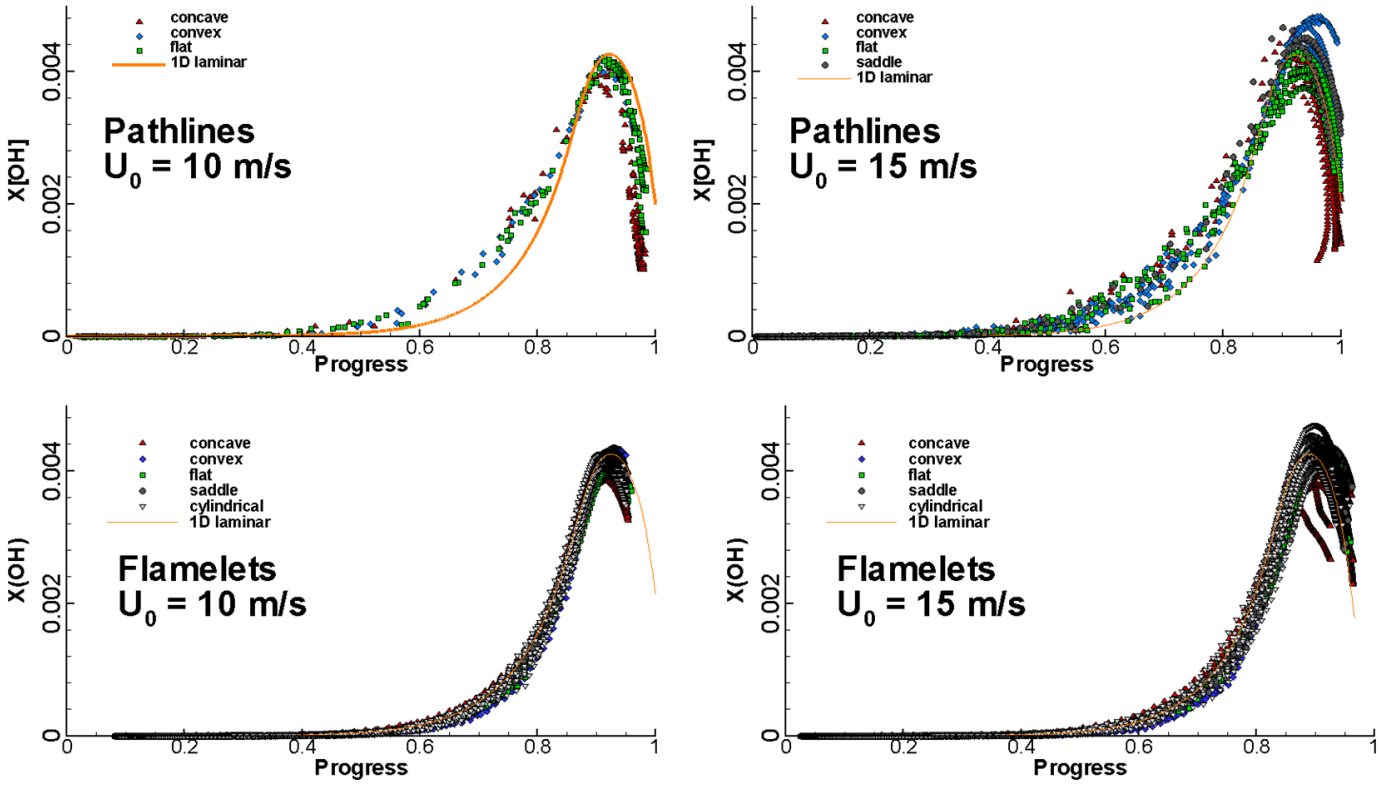

Figure 19. X[OH] as a function of progress variable on randomly selected the pathlines (top) and flamelets (bottom) representing cases M-C (left) and M-D (right).

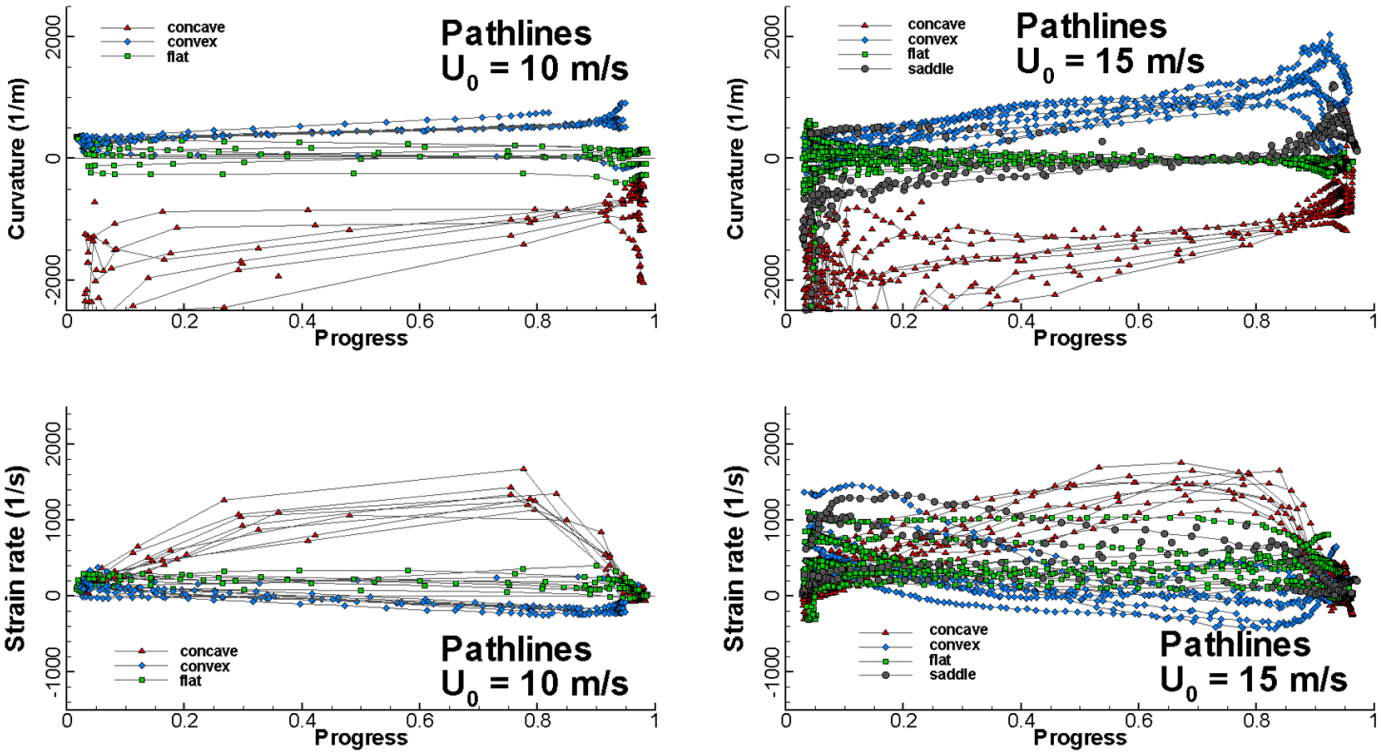

Figure 20. Curvature (top) and strain rate (bottom) along pathlines for case M-C and M-D.

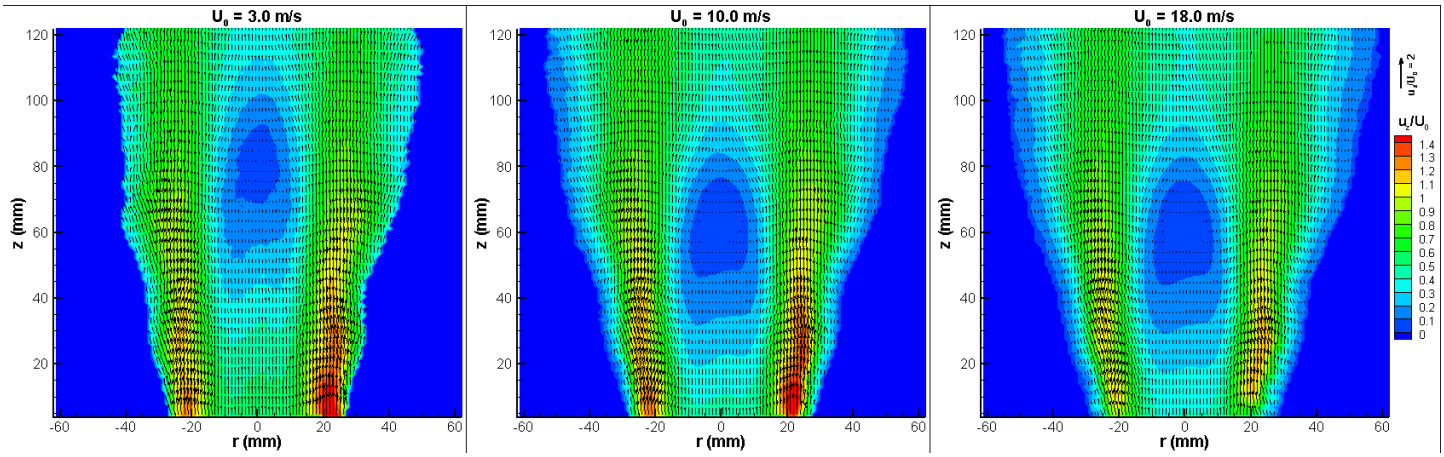

Figure A-1. 2D normalized velocity vectors of the non-reacting flows generated by the LSB at U_0 = 3, 10, and 18 m/s.

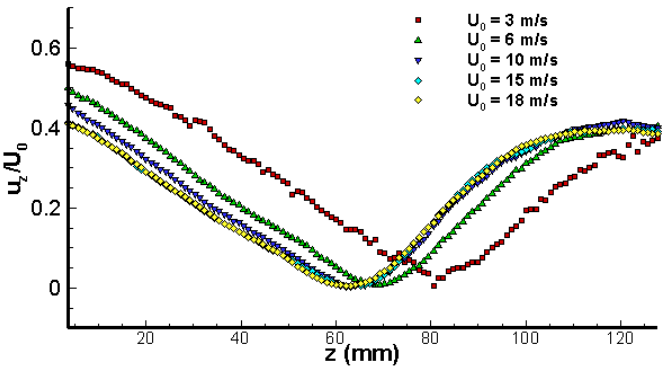

Figure A-2. Centerline normalized axial velocity profiles of the LBNL LSB non-reacting flows at U_0 = 3, 6, 10, 15 and 18 m/s corresponding to flames M-A to M-E.

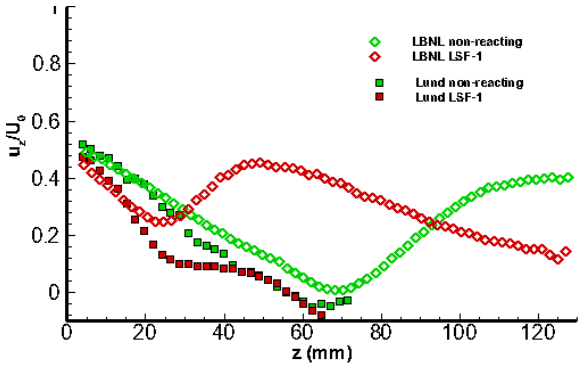

Figure A-3. Comparison of the centerline axial velocity profiles obtained at Lund and at LBNL.

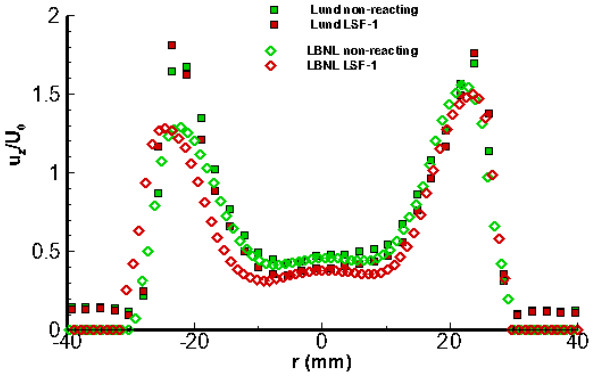

Figure A-4. Comparison of the radial profiles of the axial velocity (at $z = 10$ mm) obtained at Lund and at LBNL.